Combination of AVNIR-2, PALSAR, and Polarimetric Parameters for Land Cover Classification

Hasi Bagan, *Member, IEEE*, Tsuguki Kinoshita, and Yoshiki Yamagata

***Abstract*—We evaluate the potential of combined Advanced Land Observing Satellite Advanced Visible and Near-Infrared (AVNIR-2) and fully polarimetric Phased-Array-type L-band Synthetic Aperture Radar (PALSAR) data for land cover classification. Optical AVNIR-2 and fully polarimetric PALSAR can provide both surface spectral information and scattering information of the ground surface. The fully polarimetric PALSAR is particularly important for land cover classification because quad-polarization PALSAR data and its polarimetric parameters contain additional surface information. As a consequence, by combining optical AVNIR-2, PALSAR, and polarimetric parameters into a single data set, land cover classification accuracy may be further improved. For efficient and convenient handling of the combined multisource data, we used a subspace method for the classification and estimated its classification capability for various combinations of optical, PALSAR, and polarimetric parameter data sets in the Lake Kasumigaura region of Japan. We also compared the results obtained using the subspace method with those obtained by the support vector machine (SVM) and maximum-likelihood classification (MLC) methods. The classification results confirm that, when the combined optical AVNIR-2, PALSAR, and polarimetric coherency matrix data were used, the classification accuracy of the subspace method was better than that when other data combinations were used. The subspace method also performed better than the SVM or MLC method in high-dimensional data set classification. Moreover, the experimental results demonstrated that the proposed subspace method is robust for data classification when there is data redundancy and thus allows optimal feature selection procedures to be avoided.**

***Index Terms*—Coherency matrix, Phased-Array-type L-band Synthetic Aperture Radar (PALSAR), polarimetry, subspace method, supervised classification.**

I. Introduction

THE RECENTLY launched Advanced Land Observing Satellite (ALOS) carries both optical Advanced Visible and Near-Infrared (AVNIR-2) and fully polarimetric Phased-Array-type L-band Synthetic Aperture Radar (PALSAR) sensors. Each sensor collects a different type of surface information and thus provides a new opportunity for characterizing and mapping land cover types.

PALSAR is the first civilian spaceborne L-band fully polarimetric synthetic aperture radar (SAR) utilizing horizontally (H) and vertically (V) polarized electromagnetic waves in both transmission and reception. Different from the optical AVNIR-2, PALSAR measures the radar backscatter from both point and distributed targets on the surface, which can then be used to characterize structural properties of the surface (e.g., slope, shape, and surface roughness) and geophysical parameters (e.g., vegetation and soil moisture and salinity) [1]. Furthermore, when fully polarimetric PALSAR data are available, polarimetric target decomposition methods, including those of Cloude and Pottier [2], Freeman and Durden [3], and Yamaguchi *et al.* [4], can be used. These polarimetric target decomposition methods were developed to separate polarimetric radar scattering information into basic scattering mechanisms for such purposes as geophysical parameter inversion and terrain and target classification [5]. The different decomposition methods transform the polarimetric information into different types of scattering mechanisms [6]. The T_3 coherency matrix derived from the fully polarimetric PALSAR data has the advantage of being suitable for simple averaging to increase the equivalent number of looks and hence reduce speckle while maintaining the polarimetric phase information [7]. Various model-based decomposition methods that are exploiting the fully polarimetric information of the coherency matrix have been developed, although they are still unable to use the complete polarimetric information of the coherency matrix [5]. For minimal loss of the polarimetric information contained in the coherency matrix, it is essential to incorporate the coherency matrix directly into the classification procedure.

SAR data and optical data provide complementary information, and their combination often leads to increased classification accuracy [8]. Moreover, adding the coherency matrix to the combined data set can potentially further improve the classification accuracy. Therefore, the development of proper techniques for efficiently and conveniently handling such multilayer imbalanced image classification is becoming increasingly important.

Various approaches have been used to examine polarimetric SAR data for land cover classification: Examples include an entropy/alpha decomposition-based classification scheme used to classify different types of scattering behavior [9], a complex Wishart classifier combining a physical scattering mechanism with the statistical properties of pixels [10]–[12], a complex-valued multilayer perceptron neural network for polarimetric

Manuscript received March 7, 2011; revised June 2, 2011; accepted July 31, 2011. Date of publication September 22, 2011; date of current version March 28, 2012. This work was supported by the Research Program on Climate Change Adaptation of the Ministry of Education, Culture, Sports, Science and Technology (MEXT) of Japan.

H. Bagan and Y. Yamagata are with the Center for Global Environmental Research, National Institute for Environmental Studies, Tsukuba 305-8506, Japan (e-mail: hasi.bagan@nies.go.jp; yamagata@nies.go.jp).

T. Kinoshita is with the College of Agriculture, Ibaraki University, Ami 300-0393, Japan (e-mail: kino@mx.ibaraki.ac.jp).

Color versions of one or more of the figures in this paper are available online at http://ieeexplore.ieee.org.

Digital Object Identifier 10.1109/TGRS.2011.2164806

SAR data classification [13], the support vector machine (SVM) classification method [14], and segmentation methods [15]. Many studies have proposed the use of PALSAR data for forest type characterization [16]–[18] and cropland mapping [19] and combining PALSAR and optical data sets for land cover classification [20], [21]. Very few studies have examined the combination of fully polarimetric SAR data, polarimetric features, and optical data for classification [6]. However, as for our knowledge, the combination of fully polarimetric PALSAR data, polarimetric coherency matrix data, and optical data for classification has not previously received attention.

Recently developed subspace methods have been used to solve remote sensing image classification problems and have shown potential for efficient classification of high-dimensional remote sensing data [22]. Subspace methods have become popular both for dimensionality reduction and for building classifiers [23] because, in real-world problems, patterns are often distributed in high-dimensional nonlinear subspaces. Subspace methods aim at defining a low-dimensional subspace for each land cover class that preserves the main properties of the high-dimensional data set. Subspace methods reduce data dimensionality by incorporating feature extraction into the classification process, and they therefore have great potential for solving combined multisource remote sensing image classification problems. In this study, to demonstrate the proposed subspace classification method, we applied it to a combined multisource remote sensing image and compared its classification accuracy with accuracies obtained with two other classification techniques: a recently developed SVM [24], which is a promising machine learning methodology, and the widely used maximum-likelihood classification (MLC) method [25].

In Section II, we briefly review the fully polarimetric PALSAR data and their coherency matrix. We also present a short overview of a recently proposed subspace remote sensing data classification procedure in this section. In Section III, we present the experimental materials and methods, and in Section IV, we present and discuss the classification results. Finally, in the last section, we present our conclusions and mention some open questions to be addressed by future research.

II. Methodology

A. PALSAR Polarimetric Data

The PALSAR Level 1.1 product comprises single-look complex (SLC) data, compressed in both range and azimuth directions. The pixel spacings are 9.6 m in the range direction and 4.49 m in the azimuth direction [26]. PALSAR Level 1.1 data are composed of a real and an imaginary part (complex data) and thus contain both amplitude information and phase information of the backscattered signal from the ground surface.

In fully polarimetric PALSAR SLC data, the polarimetric behavior of a target can be described by its 2×2 complex Sinclair scattering matrix S defined by

$$S = \begin{pmatrix} S_{HH} & S_{HV} \\ S_{VH} & S_{VV} \end{pmatrix} \tag{1}$$

where the diagonal elements S_{VV} and S_{HH} are copolarized because they relate the same polarization state for the incident and backscattered fields. The off-diagonal elements S_{HV} and S_{VH} are cross polarized because they relate orthogonal polarization states [1], [27].

In the monostatic backscattering case, the scattering matrix S is assumed to be symmetrical ($S_{HV} = S_{VH}$), which means that the same amount of backscatter energy is received with the HV and VH polarizations. However, receiver noise in the radar electronics is different between the HV and the VH channels, so these channels are often averaged during data processing for more accurate measurement of the cross-polarized energy.

The scattering target vector k_p, which is preferred instead of the scattering matrix S because physical interpretation of its elements is easier (i.e., surface scattering, volume scattering, and double-bounce scattering), can be calculated from the symmetrical scattering matrix S as

$$k_p = \frac{1}{\sqrt{2}}[S_{HH} + S_{VV} \quad S_{HH} - S_{VV} \quad 2S_{HV}]^{\mathrm{T}}. \tag{2}$$

From the scattering target vector k_p, we can generate the complex coherency matrix T_3 as (3) [28], shown at the bottom of the page, where $\langle \cdot \rangle$ denotes the inner product and $k_p^{*\mathrm{T}}$ denotes the Hermitian transpose of k_p.

T_3 is a Hermitian matrix that composed of nine independent numbers: the three real diagonal elements and the three real and three imaginary parts of the three complex off-diagonal elements. These nine independent parameters are useful for general target analysis without reference to any model, and each of them contains real physical target information [1].

B. Subspace Method

The subspace method [29] has been shown to possess good generalization ability, both in theory and practice, for pattern classification [30], and modifications of the original model for remote sensing data classification have recently been presented [22]. The subspace classification procedure involves the following steps: definition of land cover classes, representation of training and test samples, pattern normalization, feature extraction to generate the subspaces, class subspace learning, and performance evaluation.

$$\begin{aligned} T_3 &= \left\langle k_p \cdot k_p^{*\mathrm{T}} \right\rangle \\ &= \frac{1}{2} \begin{bmatrix} \left\langle |S_{HH} + S_{VV}|^2 \right\rangle & \left\langle (S_{HH} + S_{VV})(S_{HH} - S_{VV})^* \right\rangle & 2\left\langle (S_{HH} + S_{VV}) S_{HV}^* \right\rangle \\ \left\langle (S_{HH} - S_{VV})(S_{HH} + S_{VV})^* \right\rangle & \left\langle |S_{HH} - S_{VV}|^2 \right\rangle & 2\left\langle (S_{HH} - S_{VV}) S_{HV}^* \right\rangle \\ 2\left\langle S_{HV}(S_{HH} + S_{VV})^* \right\rangle & 2\left\langle S_{HV}(S_{HH} - S_{VV})^* \right\rangle & 4\left\langle |S_{HV}|^2 \right\rangle \end{bmatrix} \end{aligned} \tag{3}$$

The subspace method is a supervised classification method in which each pixel is represented in terms of d features or measurements and is viewed as a point in a d-dimensional space.

Given a set of training samples from each class, the objective is to establish subspaces in the feature space that separate samples belonging to different class subspaces. The effectiveness of the subspace is determined by how well samples from different classes can be separated.

Assume that labeled training samples $\{X_{i,j}\}$ $(i = 1, \ldots, c;$ $j = 1, \ldots, p_i)$ belong to c categories $\omega_1, \omega_2, \ldots, \omega_c$, where p_i is the total number of training samples in class ω_i. Each sample is a d-dimensional $(=$ bands$)$ vector.

In the preprocessing step, the training patterns are normalized as follows: For a given pixel $X_{i,j} = (x_1, x_2, \ldots, x_d)^{\mathrm{T}}$ of category ω_i, the normalized pixel is computed as

$$X_{i,j} = (x_1/L, x_2/L, \ldots, x_d/L)^{\mathrm{T}} \tag{4}$$

where $L = \sqrt{x_1^2 + x_2^2 + \cdots + x_d^2}$ is the norm (length) of the vector that represents the given pixel $X_{i,j}$. For the sake of brevity, we also use $X_{i,j}$ to denote the normalized pixel.

Next, the normalized training data set is used to determine the appropriate class subspace of dimensionality m ($m < p_i$, with $i = 1, 2, \ldots, c$) in the original feature space of dimensionality d ($m < d$). For example, in class ω_i, the m largest eigenvectors of the $d \times d$ correlation matrix of P_i d-dimensional patterns are computed

$$P_i = \sum_{j=1}^{p_i} X_{i,j}^{\mathrm{T}} X_{i,j} \tag{5}$$

where P_i is the $d \times d$ correlation matrix. Then, principal component analysis is used to compute the m largest eigenvalues and the corresponding eigenvectors of the class correlation matrix. The m eigenvectors corresponding to the largest m eigenvalues span the class ω_i subspace.

Let the m largest eigenvalues of P_i be arranged in descending order and the corresponding eigenvectors be denoted by $\{V_{i,j} | j = 1, \ldots, m\}$ $(m < d)$; here, m equals the subspace dimension of class ω_i.

The similarity of a normalized image pixel x to this class ω_i is computed as the weighted orthogonal projection length

$$g_i(x) = \sum_{j=1}^{m} \left(\lambda_i^{(j)} / \lambda_i^{(1)}\right)^{\rho} \left[x^{\mathrm{T}} V_{i,j}\right]^2 \tag{6}$$

where ρ is a small nonnegative constant value parameter and $\{\lambda_i^{(j)} | j = 1, \ldots, m\}$ are the first m largest eigenvalues of the correlation matrix in descending order. Pixel x is then classified into the class with the largest projection length.

However, there may be some overlap between the initially obtained subspaces, which decreases the classification accuracy. To separate patterns belonging to different classes, the learning subspace method has been proposed to reduce this subspace overlap.

The averaged learning subspace method (ALSM) is the most commonly used learning subspace method. We briefly describe the ALSM here. In ALSM, the class correlation matrices are modified with each learning iteration, and then, the basis vectors of the subspaces are updated.

In each iteration step t, all training samples are first classified using (6) according to the currently existing subspaces. Then, the misclassified training samples are divided according to the misclassification type: A sample vector of class ω_i may be misclassified into another class, for example, ω_j, or a sample vector of another class, for example, ω_k, may be misclassified into class ω_i. Thus, we need to compute the following two types of conditional correlation matrices $P_t^{(i,\mathrm{out})}$ and $P_t^{(i,\mathrm{in})}$ $(1 \le i \le c)$:

$$P_t^{(i,\mathrm{out})} = \sum_j Y_{i,j}^{\mathrm{T}} Y_{i,j} \tag{7}$$

when $Y_{i,j}$ $(1 \le i \le c;\ 1 \le j \le p_i)$ belongs to class ω_i but is mislabeled into another class, and

$$P_t^{(i,\mathrm{in})} = \sum_{k \ne i} \sum_j Z_{k,j}^{\mathrm{T}} Z_{k,j} \tag{8}$$

when $Z_{k,j}$ $(1 \le k \le c;\ 1 \le j \le p_k)$ belongs to class ω_k $(k \ne i)$ but is mislabeled into class ω_i.

Next, we generate a new correlation matrix of class ω_i

$$P_t^{(i)} = P_{t-1}^{(i)} + \alpha P_t^{(i,\mathrm{out})} - \beta P_t^{(i,\mathrm{in})}. \tag{9}$$

Here, $P_0^{(i)} = P_i$, and α and β are the learning parameters, which are usually set to two constant values that do not vary during the iteration process. Then, the m largest eigenvectors of $P_t^{(i)}$, corresponding to the largest m eigenvalues, are computed to span the updated class ω_i subspace. The iterations of the learning procedure terminate when the predefined condition is achieved.

Several parameters need to be set, namely, the learning parameters α and β, the parameter ρ, and the number of dimensions of each subspace. If the subspace dimensions for each class are the same and the two learning parameters are equal, the accuracy of recognition is optimized [31]. Thus, we set the dimensions of the subspaces of each class to the same value rather than set the dimensions of each subspace independently. Furthermore, we set both learning parameters to the same constant value. The optimal parameter values can be easily determined by an automatic optimization system [32].

III. Materials and Methods

A. Study Area

The study area was the Lake Kasumigaura region of Japan (Fig. 1), approximately 70 km northeast of Tokyo near the Japan Aerospace Exploration Agency (JAXA). The climate is characterized by high humidity and warm temperatures. The annual average air temperature is about 14 °C, and the annual precipitation is 1250 mm. Most of the study area is almost flat plain with altitudes between −2 m (reclaimed lands below sea level) and 30 m above sea level, except for flat-topped Mount Tsukuba in the northwestern study area, where the highest point is about 870 m above sea level. This area has a large diversity of land cover types, which have been extensively documented by *in situ* survey. The main land use/land cover types represented are forests, paddy fields, croplands, lotus fields, grasslands, golf courses, parks, settlements (both urban and suburban areas),

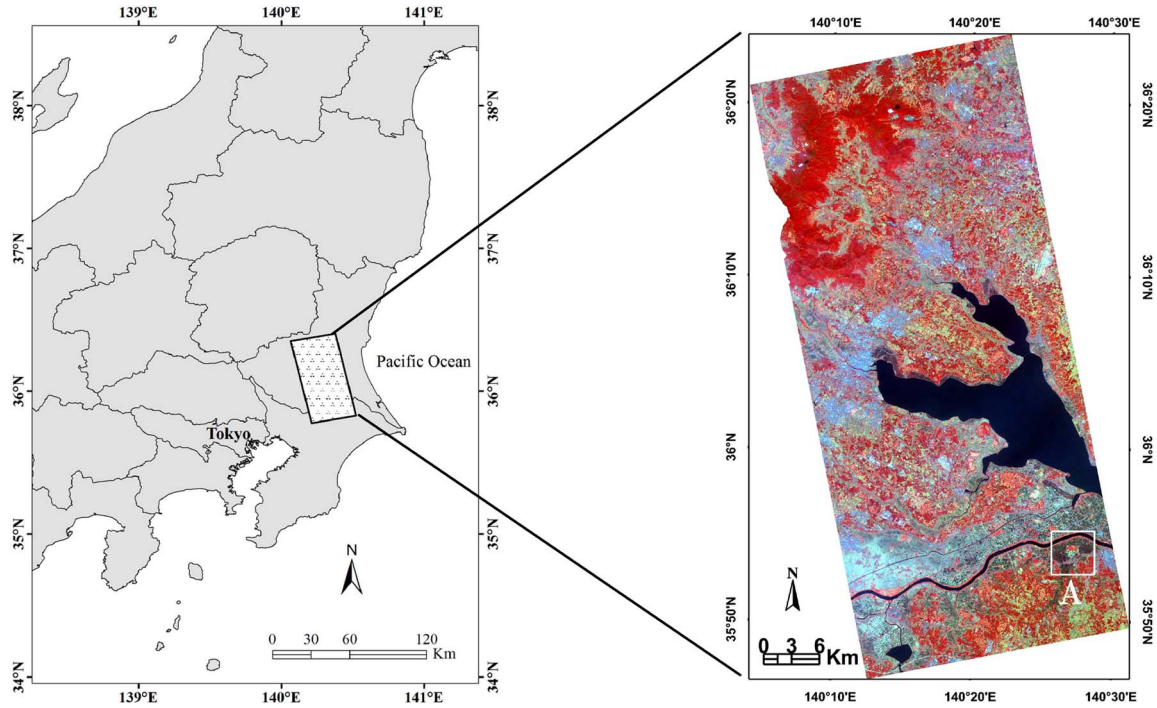

Fig. 1. False-color composite AVNIR-2 image (RGB = bands 4, 3, and 1) of the study area acquired on April 13, 2009, and its location in the Lake Kasumigaura region, Japan. The square labeled "A" indicates the area shown in the images in Fig. 4.

and water (rivers and lakes). Rice in this area is grown on flood plains, in coastal areas, and in narrow strips along small upland rivers that become narrower upstream [33]. Paddy fields are plowed using farm machines several times before being flooded by shallow water at the end of April. In this region, the rice seedlings are transplanted in the first week of May. Some parts of paddy fields may be flooded by shallow water during April if the water level in an adjacent river rises above the paddy field elevation.

B. Remotely Sensed Data

1) AVNIR-2: An ALOS AVNIR-2 (three visible and one near-infrared bands) image acquired on April 13, 2009, over the study area was used in this work (Fig. 1). The spatial resolution of the four AVNIR-2 bands was approximately 10 m, but these data were resampled to 15 m using the cubic convolution method done by JAXA. We rectified the ALOS AVNIR-2 image by using ground control points (GCPs) from Digital Map 2500 (Spatial Data Framework; scale of 1:2500) published by the Geographical Survey Institute, Japan. GCPs were well dispersed and yielded a root-mean-square (rms) error of 0.59 pixel. The image contained no visible distortion, haze, clouds, or shadows, excepting two small clouds and their corresponding shadows over Mount Tsukuba (northwestern study area).

2) PALSAR: Full-scene L-band PALSAR Level 1.1 SLC data were acquired on April 7, 2009, in quad-polarization mode (HH, HV, VH, VV) in an ascending orbit with an incidence angle of 21.5°.

The standard Level 1.1 product produced by JAXA was converted to a normalized radar cross section as follows:

$$\sigma^0_{1.1\,\text{product}} = 10\log_{10}\langle I^2 + Q^2\rangle + CF - A \qquad (10)$$

where I and Q are the real and imaginary parts of the SLC data. The conversion factor CF is -83.0, and A is 32.0 [22]. Here, instead of (10), we used the following equation to convert the four-channel PALSAR Level 1.1 data:

$$\sigma^0_{1.1\,\text{product}} = 10\log_{10}\langle I^2 + Q^2\rangle + B. \qquad (11)$$

Here, we set B to 80 to avoid the negative value and make it easy to tune the learning parameters in (9). This kind of linear conversion does not affect the classification accuracy.

The coherency matrix T_3 contains additional real physical target information over that contained in the converted PALSAR four-channel data. Therefore, we incorporated the nine independent elements of the coherency matrix (i.e., the three real diagonal elements and the real and imaginary parts of the three off-diagonal elements) into the classification process in order to achieve more meaningful land cover information.

The PALSAR data were processed using the ENVI SARscape (ITT VIS SARscape) SAR processor and in-house software. The PALSAR four-channel data and the nine elements of the T_3 coherency matrix were preprocessed as follows: 4×1 multilooking; reduction of speckle effects with a window size of 5×5 refined Lee filter; and geocoding and terrain correction using the 90-m-spatial-resolution Shuttle Radar Topography Mission (SRTM-3) elevation data. In addition, the PALSAR four-channel data processing also included radiometric calibration and normalization. Finally, we added 50 to the nine elements of the coherency matrix T_3 to avoid the negative value. All data were geocoded to 15 m to match the spatial resolution of the AVNIR-2 data and coregistered with respect to the AVNIR-2 data in order to achieve meaningful land cover information and minimize misregistration errors. In particular, the PALSAR four-channel data and the nine elements of the coherency matrix T_3 were

TABLE I
LAND COVER CLASSES AND PIXEL COUNTS IN THE LAKE KASUMIGAURA REGION OF JAPAN

Land Cover Class	Class Description	Training Pixel Count	Test Pixel Count
1. Urban/Built-up	Buildings, concrete, and other human-made structures	1463	861
2. Forest	Forests (canopy cover more than 50%)	1609	1079
3. Water	Rivers and lakes	1307	829
4. Paddy	Plowed paddy fields before flooding	1814	867
5. Wheat	Winter wheat	1079	781
6. Flooded paddy	Plowed paddy fields flooded by shallow water	1107	571
7. Lotus	Lotus fields	773	452
8. Cropland	Dry croplands	1111	573
9. Grassland	Dominated by dense grass or shrubs	1040	624
10.Sparse	Sparse vegetation areas: e.g., parks, golf courses, playing fields	1012	585
11. Road	Asphalt paved road	947	551
Total		13262	7773

TABLE II
FIVE DATA SET GROUPS USED FOR CLASSIFICATION

Group	Data	Designation	Total number of bands	Pixel size
G1	AVNIR-2	Bands 1–4	4	15 m
G2	AVNIR-2, PALSAR	Bands 1–4, *HH*, *HV*, *VH*, *VV*	8	15 m
G3	AVNIR-2, T3	Bands 1–4, T_{11}, T_{22}, T_{33}, Re(T_{12}), Im(T_{12}), Re(T_{13}), Im(T_{13}), Re(T_{23}), Im(T_{23})	13	15 m
G4	AVNIR-2, PALSAR, six elements of T3	Bands 1–4, *HH*, *HV*, *VH*, *VV*, Re(T_{12}), Im(T_{12}), Re(T_{13}), Im(T_{13}), Re(T_{23}), Im(T_{23})	14	15 m
G5	AVNIR-2, PALSAR, T3	Bands 1–4, *HH*, *HV*, *VH*, *VV*, T_{11}, T_{22}, T_{33}, Re(T_{12}), Im(T_{12}), Re(T_{13}), Im(T_{13}), Re(T_{23}), Im(T_{23})	17	15 m

coregistered by using GCPs from the rectified AVNIR-2 data and applying a polynomial transformation. The rms error was 0.68 pixel.

3) Ancillary Data: We conducted an extensive field survey from April 6 to 15, 2009, and from September 21 to 24, 2010, in order to gather field-based land cover observations. In addition to the field survey data, the following remote sensing and geographic information system (GIS) data sets were used for determination of typical land cover classes and field training sites: IKONOS satellite images acquired during 2004–2007; GeoEye-1 satellite image acquired on April 23, 2009; ALOS AVNIR-2 images acquired on October 16, 2008, May 20, 2009, and August 29, 2009; and Digital Map 2500 (Spatial Data Framework; scale of 1:2500) published by the Geographical Survey Institute, Japan. Using the field investigation results, the visual interpretation of the remote sensing and GIS data sets, we designated 11 ground-cover types in this experiment (Table I). The training and test samples were randomly selected from separate local patch data by manual digitization in order to ensure that they were spatially disjoint and to reduce any potential correlation between the training and test data [34].

To evaluate how different source data sets contributed to classification accuracy, we set up five data set groups designated G1–G5 (Table II).

In these groups, T_{11}, T_{22}, and T_{33} denote the three real diagonal elements; Re(T_{12}), Re(T_{13}), and Re(T_{23}) denote the real parts of the three off-diagonal elements; and Im(T_{12}), Im(T_{13}), and Im(T_{23}) denote the imaginary parts of the three off-diagonal elements, of the coherency matrix T_3.

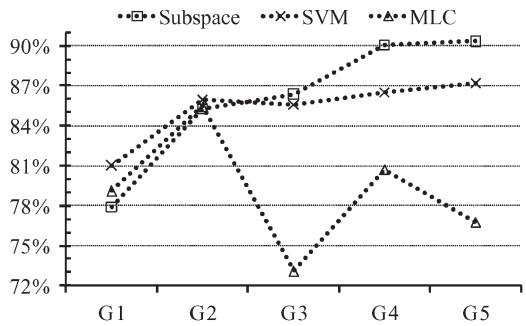

Fig. 2. Classification accuracy of the subspace method increased more rapidly than those of the MLC and SVM methods as the number of bands increased.

From (3), it can be seen that T_{33} has a high correlation with PALSAR channels HV or VH, and T_{11} and T_{22} have a high correlation with PALSAR channels HH and VV. G5 contains both the four PALSAR channels and the nine elements of T_3 to allow evaluation of the classifiers when there is data redundancy.

IV. RESULTS AND DISCUSSION

The subspace, SVM, and MLC methods were each applied to the five data set groups (Table II), and the overall accuracies of

TABLE III
CLASSIFICATION ACCURACIES OF LAND COVER MAPS OBTAINED WITH EACH OF THE FIVE DATA SET GROUPS, SHOWN BY THE PRODUCER'S AND USER'S ACCURACIES FOR EACH LAND COVER CLASS AND THE OVERALL ACCURACY AND THE KAPPA COEFFICIENT

Class	G1						G2						G3						G4						G5					
	MLC		*SVM*		*Subspace*		*MLC*		*SVM*		*Subspace*		*MLC*		*SVM*		*Subspace*		*MLC*		*SVM*		*Subspace*		*MLC*		*SVM*		*Subspace*	
	Prod.	User	Prod.	User	Prod.	User	Prod.	User	Prod.	User	Prod.	User	Prod.	User	Prod.	User	Prod.	User	Prod.	User	Prod.	User	Prod.	User	Prod.	User	Prod.	User	Prod.	User
1.Urban	33.22	81.71	72.24	68.28	38.21	72.47	79.21	92.04	92.45	93.76	62.25	93.38	85.37	86.67	92.92	95.35	77.24	91.72	74.22	86.82	92.33	93.97	88.27	94.88	85.13	87.26	94.66	94.66	91.06	95.84
2.Forest	99.54	99.17	100	98.81	99.44	98.99	99.91	99.35	99.63	98.62	100	98.63	99.81	97.29	100	99.45	98.98	99.63	99.91	98.63	99.91	98.99	100	99.36	99.72	96.68	99.91	99.45	99.91	99.35
3.Water	80.1	99.55	85.28	96.85	83.84	95.21	78.29	98.63	85.52	95.68	81.3	93.35	46.8	96.76	85.89	97.27	86.49	94.09	74.07	97.46	85.16	96.19	88.18	97.34	52.59	97.32	85.4	96.46	89.14	94.26
4.Paddy	79.12	89.67	86.97	85.29	86.04	68.69	82.81	96.51	83.04	95.11	92.85	73.99	33.56	82.2	81.31	89.02	88.81	88	67.7	90.73	84.08	95.42	92.27	95.58	55.71	86.87	84.66	95.32	93.54	96.2
5.Wheat	81.43	81.64	74.39	82.29	87.45	78.33	80.92	85.64	72.47	85.5	94.88	85.17	76.7	87.96	76.82	84.27	95.13	80.67	79.26	86.09	73.62	85.31	94.11	84.39	77.34	89.09	76.95	86.98	92.7	84.19
6.F.Paddy	80.39	85	81.79	80.8	80.04	75.41	81.79	87.45	80.56	79.45	83.36	84.1	74.43	75.76	84.06	81.36	88.62	80.7	78.11	77.3	84.24	81.39	88.09	84.11	75.31	75.44	85.81	83.33	92.12	84.7
7.Lotus	83.85	63.48	79.65	68.05	77.21	63	87.83	66.06	82.96	69.7	82.52	66.25	79.87	45.93	80.31	69.14	75.44	72.55	80.53	65.59	83.63	71.32	83.85	75.8	81.42	50.48	82.74	70.97	80.53	79.82
8.Crop	98.43	95.59	97.91	97.06	91.45	98.68	98.6	97.41	98.08	97.06	95.99	93.86	97.03	86.74	98.08	98.08	98.08	95.58	97.73	92.11	98.25	97.24	98.95	96.1	97.91	89.33	98.78	96.92	98.25	98.25
9.Grass	74.84	60.97	73.56	59.38	61.22	64.86	81.09	64.05	80.29	59.93	72.28	87.23	66.35	52.14	76.6	60.51	63.46	76.74	68.59	60.62	79.65	60.39	72.6	81.04	69.87	54.03	80.45	61.82	70.83	78.51
10.Sparse	75.56	94.65	78.12	89.26	85.13	83.98	77.26	94.36	77.95	93.44	91.62	92.57	57.95	75.84	75.73	89.49	85.47	88.34	74.19	81.58	77.78	93.62	88.72	93.18	59.32	78.86	74.7	91.81	87.35	91.58
11.Road	89.47	42.17	45.74	52.5	58.26	47.63	90.2	60.39	83.67	70.49	74.05	66.45	90.56	43.28	77.86	67.03	80.94	68.51	91.47	51.96	84.39	70.78	86.21	76.24	89.66	51.24	85.84	73.22	87.11	78.43
O. A.	*79.12*		*81.04*		*77.92*		*85.46*		*85.95*		*85.28*		*73.12*		*85.57*		*86.38*		*80.70*		*86.48*		*90.07*		*76.78*		*87.20*		*90.34*	
Kappa	*0.7698*		*0.7901*		*0.7559*		*0.8394*		*0.8447*		*0.8372*		*0.7042*		*0.8404*		*0.8493*		*0.7870*		*0.8505*		*0.8901*		*0.7440*		*0.8585*		*0.8931*	

Notes: Prod. indicate the Producer's accuracy, User indicate the User's accuracy, O.A indicate the Overall accuracy and Kappa indicate the Kappa coefficient.

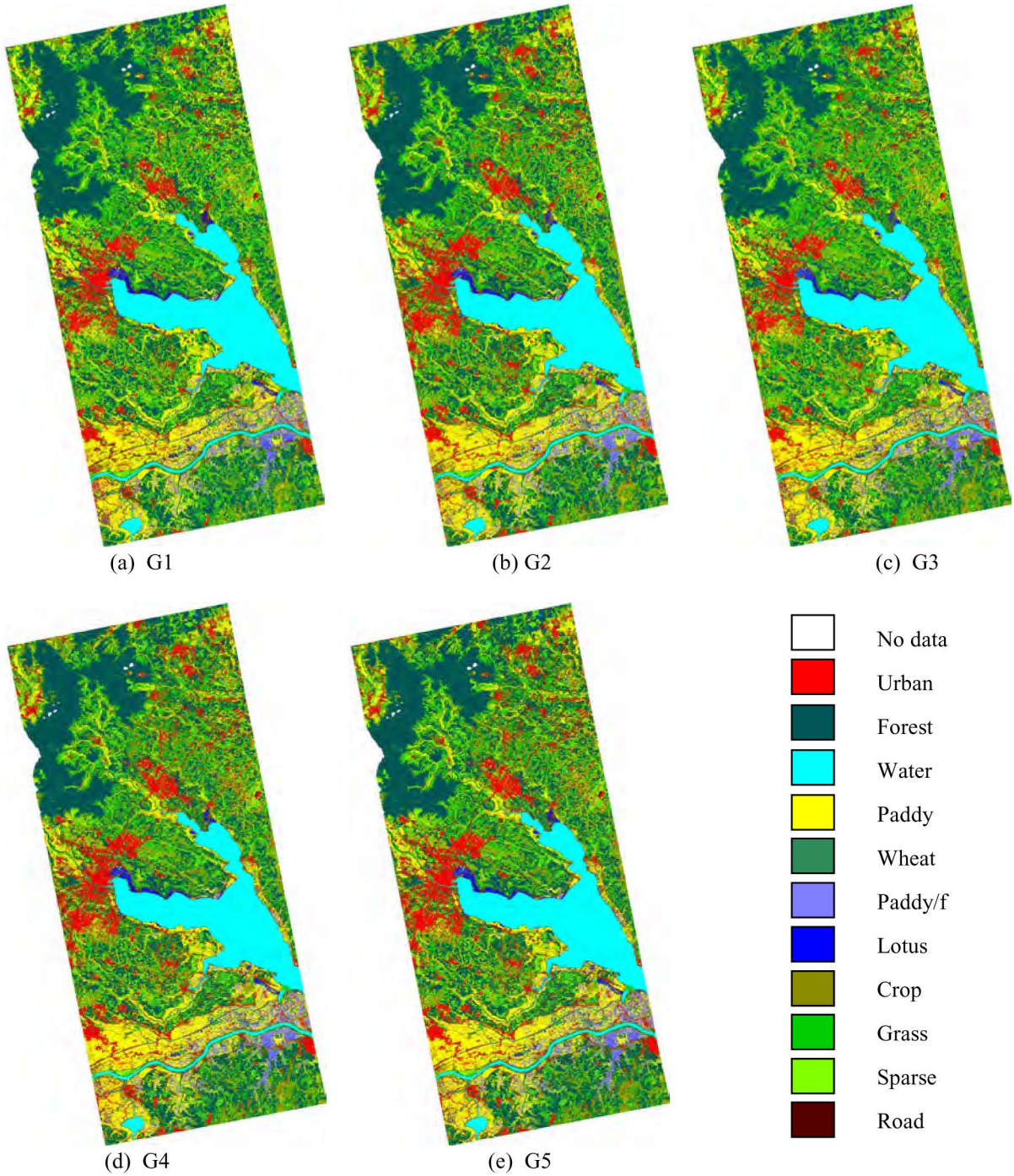

Fig. 3. Land cover classification maps obtained with (a) G1 by SVM, (b) G2 by SVM, (c) G3 by subspace, (d) G4 by subspace, and (e) G5 by subspace in the Lake Kasumigaura area of Japan.

the methods with the different data set groups were compared (Fig. 2).

As expected, classification performance clearly benefited from multisource data fusion. The best classification result was obtained with the subspace method when the full G5 data set was used. With the subspace method, the classification accuracy tended to increase with the use of more data source types (Fig. 2). With SVM, the trend was similar, but the subspace method classification performance was better than the SVM performance with the G3, G4, and G5 groups. All three of the classification methods achieved better classification results with the G2 data set than with the optical-only G1 data set. With the G1 data set group, either the three classification methods could not separate urban and road classes or the accuracy was considerably lower.

The parameters that were used to build the best classifiers were provided. The number of subspace dimensions and the optimal number of training iterations in the subspace were 4 and 747 for G3, 4 and 943 for G4, and 7 and 960 for G5, respectively. The SVM classifier with Gaussian radial basis

function (RBF) kernels in ENVI software (ITT VIS version 4.7) is used in this study. Although the RBF kernel function is widely accepted in remote sensing applications, the SVM algorithm with an RBF kernel was a significantly time-consuming procedure for handling large data sets with high dimensionality [35], [36]. Therefore, we chose trial-and-error testing instead of an automatic parameter optimization technique for SVM with an RBF kernel. For further information regarding the parameter selection and optimization technique of the SVM algorithm, please refer to [36]–[38]. The trial-and-error testing showed that the best values for the gamma (width) and penalty parameters were 0.2 and 120 with G1 and 0.1 and 150 with G2, respectively.

Comparison of the three methods (Fig. 2) showed that, with the G1 data set group (four bands) and the G2 group (eight bands), the classification accuracy of the SVM method was better than that of the MLC or subspace method. However, with the high-dimensional G3 (13 bands), G4 (14 bands), and G5 (17 bands) data set groups, the subspace method results were more accurate than those obtained by the SVM and MLC methods. SVM tries to find an optimal hyperplane that maximizes the margin between classes, which then minimizes the misclassification error on the training set. However, a previous study reveals that the accuracy of a classification by an SVM does vary as a function of the number of features used [24], [37]. When the number of features is large, the highly correlated features may have a negative impact on classification accuracy [38]. Therefore, SVM had the highest performance for low-dimensional G1 and G2, but it had difficulties in constructing an effective classifier model from relatively high dimensional data sets of G3, G4, and G5. In contrast, for the subspace method of high-dimensional data classification, the overlap between low-dimensional class subspaces is reduced enough in the high-dimensional space, and thus, the performance using the subspace method on G3, G4, and G5 made it outperform relative to MLC and SVM, while the lower MLC results are probably due to the MLC assumption of equal prior probability (likelihood) of occurrence for each class [25] and the MLC apportion of pixels into a class regardless of distance from class mean. When the subspace method was used, the classification accuracy was the highest with the combination of AVNIR-2 and PALSAR data and all nine elements of the coherency matrix (G5), but the classification accuracy was nearly as high when the AVNIR-2 and PALSAR data and six elements of the coherency matrix (G4) were used. The classification accuracy of the SVM method showed a similar trend, but the classification accuracies obtained with the G4 and G5 data set groups were considerably lower than those obtained with the subspace method.

The confusion matrix (error matrix) tallies how the classification process has labeled a series of test pixels at which the correct land cover label is known [34]. To assess the quality of the image classifications, confusion matrices comparing test pixels (Table I) to the classification results obtained by the MLC, SVM, and subspace methods were created, and the overall accuracy, producer's accuracy, user's accuracy, and kappa coefficient of agreement (or κ statistic) were generated (Table III).

With the AVNIR-2 optical image (G1), the overall accuracy was only 81.0%, and the corresponding κ statistic was 0.79 (Table III). However, the addition of the four PALSAR channels to the optical image (G2) caused the overall classification accuracy to increase rapidly to 86.0%, and the corresponding κ statistic was 0.84; furthermore, the highest classification accuracy of 90.3% (κ statistic of 0.89) was obtained when all AVNIR-2 and PALSAR channels, as well as all nine elements of the coherency matrix (G5), were used.

On the G1 group, the subspace method gives the lowest overall classification accuracy (Table III). As we mentioned earlier, the reason is mainly due to the overlap between class subspaces in the low-dimensional data space (G1). One possible solution is to map the data space into a higher dimensional feature space by kernel-based methods in order to reduce the overlap between subspaces while maintaining computational simplicity of the subspace learning procedure.

Fig. 3 shows the best classification maps obtained by the subspace or SVM method with G1–G5. As expected, the topographic variations in the Mount Tsukuba area had limited impact on the classification performance because this area is almost entirely covered by forest.

Overall, the best classification results among the five data set groups were obtained with G5. With subspace for G5 (Table III and Fig. 3), the producer's accuracies (reflecting errors of omission) of majority land cover classes were notably increased compared with the other data set groups. The lowest producer's accuracy with G5, for grassland (70.8%), was due to misclassification of grassland into sparse or wheat. The producer's accuracy of lotus was 80.5% due to misclassification of lotus into flooded paddy or water. The user's accuracy (reflecting errors of commission) of most classes, except lotus, grassland, and road, was over 84% with G5. That of grassland was the lowest (78.5%) due to sparse and wheat being misclassified as grassland, and that of lotus was 79.8% due to the misclassification of water and flooded paddy. The user's accuracy of road was just 78.4%, but this value was nevertheless notably larger than the user's accuracies obtained with the other data set groups.

The combination of AVNIR-2 and PALSAR data (best classifiers for G1–G5) did not improve or decrease the accuracies of grassland and lotus compared with G1 (Table III). The classification errors of these land cover classes were caused mainly by their spectral similarities on AVNIR-2 images and their similar surface structural properties and physical parameters in PALSAR data [8]. Further research is needed to develop better rules to improve the classification accuracies of these classes when AVNIR-2 and PALSAR data are used in combination for the classification.

To visualize the differences in the classified regions more clearly, we examined the land cover images at location *A* in greater detail (see Fig. 1). Location *A* is a typical agricultural region (Fig. 4), with a few built-up areas consisting mostly of single-family houses and including some trees. We examined six images of location *A*: GeoEye-1 with a spatial resolution of 2 m (RGB = red, green, and blue bands) and the five land cover classification maps obtained with G1–G5.

Some land cover classes that were confused when G1 (AVNIR-2) was used were separated when G2 was used for the classification. For example, with G1, urban and road classes were confused with each other or were misclassified into paddy or grassland. The two classes were easily separated from each

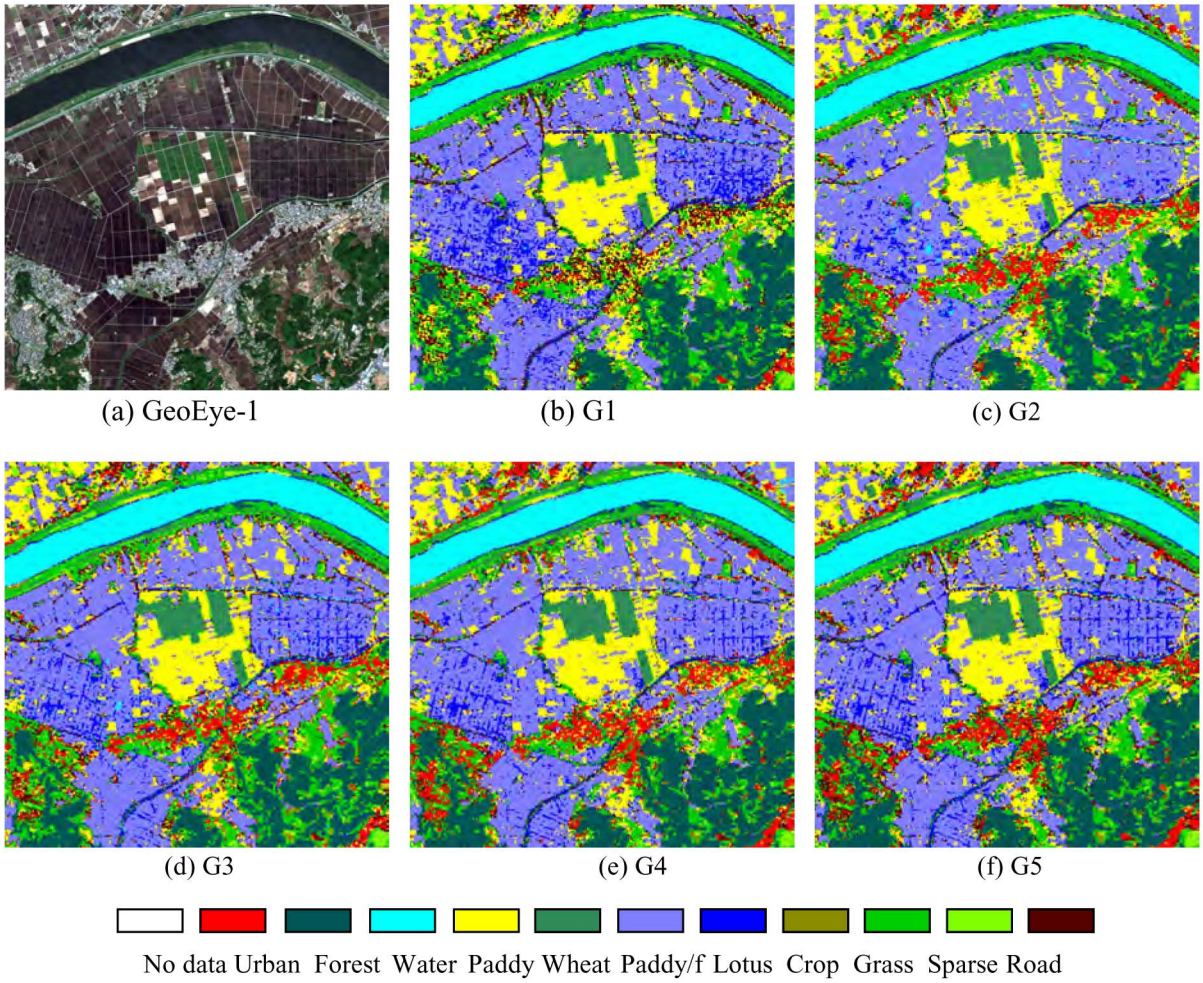

Fig. 4. Images and classification maps of location *A* (see Fig. 1): (a) GeoEye-1, (b) G1, (c) G2, (d) G3, (e) G4, and (f) G5 data set groups.

other and from paddy and grassland with G2 because urban has a very high backscatter and road has a very low backscatter. Furthermore, the addition of the coherency matrix in G4 and G5 markedly improved the discrimination between classes. The urban and road classification accuracies in particular were very impressively improved when additional polarimetric parameters were taken into account, mainly because the coherency matrix provided additional information about the backscatter behavior (e.g., phase, etc.) of the surface targets.

The performance of the subspace method with the high-dimensional G4 and G5 data set groups demonstrates that the subspace method is robust when there is data redundancy. This implies that the subspace method can avoid problems associated with the optimal feature selection procedure.

Aside from the five data set groups (G1–G5), the following three data sets were also evaluated in terms of the overall accuracy. Those are 4-band (HH, HV, VH, and VV) radar data, 13-band (HH, HV, VH, VV, and T_3) radar data, and a composite 5-band image (4-band AVNIR-2 data combining with AVNIR-2-derived Normalized Difference Vegetation Index). We found that the overall classification accuracies of both 4- and 13-band radar data were lower than 50% using 11 classes by MLC, SVM, and subspace, respectively. The producer's classification accuracies of the grassland and sparse classes were lower than 20%. It indicates that only using the radar data could not separate the two classes in this case. For the composite five-band image, the best result obtained by SVM on the five-band image was 81.36%, corresponding to a slight gain of +0.32%, compared with that achieved by the four-band AVNIR-2 data. As the classification accuracy was not improved dramatically, the topic of combining NDVI into the classification was not addressed in this paper but will be investigated in the near future.

V. Conclusion

In this paper, we have examined the use of the combination of AVNIR-2 and PALSAR data with polarimetric parameters for land cover classification by a subspace classification approach. Our results confirm that fully polarimetric PALSAR data improve the accuracy of the land cover classifications and that classification using the combined data sets has a clear advantage over optical-sensor-based classification. These classification results could be further improved by introducing optimal image-derived vegetation indices, texture information, and PALSAR-derived polarimetric decompositions into composite products to better represent variability. Additionally, it may be possible to improve the multisource combined data classification by introducing a weight parameter of individual bands to

better represent the influence of individual bands (or groups of bands).

Our comparative analysis confirmed that the performance of the subspace method was much better than that of SVM or MLC when high-dimensional combined multisource remote sensing images were used. Further research should improve the subspace learning rules to allow the training procedures to achieve more stable convergence. For example, turning the learning parameter values of α and β into learning parameter vectors corresponds to a respective weighing of each class that also involves the class influences in the training process. In addition, we can also expect a further improvement of subspace classification by introducing nonlinear dimensionality reduction techniques [39] into the subspace training stage. These were not the focus of our work for this paper. We, however, are interested in collaborations with other researchers to further develop these techniques.

REFERENCES

[1] J. S. Lee and E. Pottier, *Polarimetric Radar Imaging: From Basics to Applications*. New York: CRC Press, 2009.

[2] S. R. Cloude and E. Pottier, "A review of target decomposition theorems in radar polarimetry," *IEEE Trans. Geosci. Remote Sens.*, vol. 34, no. 2, pp. 498–518, Mar. 1996.

[3] A. Freeman and S. L. Durden, "A three-component scattering model for polarimetric SAR data," *IEEE Trans. Geosci. Remote Sens.*, vol. 36, no. 3, pp. 963–973, May 1998.

[4] Y. Yamaguchi, T. Moriyama, M. Ishido, and H. Yamada, "Four component scattering model for polarimetric SAR image decomposition," *IEEE Trans. Geosci. Remote Sens.*, vol. 43, no. 8, pp. 1699–1706, Aug. 2005.

[5] J. S. Lee and T. L. Ainsworth, "The effect of orientation angle compensation on coherency matrix and polarimetric target decompositions," *IEEE Trans. Geosci. Remote Sens.*, vol. 47, no. 1, pp. 53–64, Jan. 2011.

[6] M. Shimoni, D. Borghys, R. Heremans, C. Perneel, and M. Acheroy, "Fusion of PolSAR and PolInSAR data for land cover classification," *Int. J. Appl. Earth Obs. Geoinf.*, vol. 11, no. 3, pp. 169–180, Jun. 2009.

[7] I. H. Woodhouse, *Introduction to Microwave Remote Sensing*. New York: Taylor & Francis, 2006.

[8] Y. Ban, H. Hu, and I. Rangel, "Fusion of QuickBird MS and RADARSAT SAR data for urban land-cover mapping: Object-based and knowledge-based approach," *Int. J. Remote Sens.*, vol. 31, no. 6, pp. 1391–1410, Mar. 2010.

[9] S. Cloude and E. Pottier, "An entropy based classification scheme for land applications of polarimetric SAR," *IEEE Trans. Geosci. Remote Sens.*, vol. 35, no. 1, pp. 68–78, Jan. 1997.

[10] J. S. Lee, M. Grunes, and R. Kwok, "Classification of multi-look polarimetric SAR imagery based on complex Wishart distribution," *Int. J. Remote Sens.*, vol. 15, no. 11, pp. 2299–2311, 1994.

[11] L. Ferro-Famil, E. Pottier, and J.-S. Lee, "Unsupervised classification of multifrequency and fully polarimetric SAR images based on the H/A/alpha–Wishart classifier," *IEEE Trans. Geosci. Remote Sens.*, vol. 39, no. 11, pp. 2332–2342, Nov. 2001.

[12] A. Lönnqvist, Y. Rauste, M. Molinier, and T. Häme, "Polarimetric SAR data in land cover mapping in boreal zone," *IEEE Trans. Geosci. Remote Sens.*, vol. 48, no. 10, pp. 3652–3662, Oct. 2010.

[13] R. Hänsch, "Complex-valued multi-layer perceptrons—An application to polarimetric SAR data," *Photogramm. Eng. Remote Sens.*, vol. 76, no. 9, pp. 1081–1088, Sep. 2010.

[14] C. Lardeux, P.-L. Frison, C. Tison, J.-C. Souyris, B. Stoll, B. Fruneau, and J.-P. Rudant, "Support vector machine for multi-frequency SAR polarimetric data classification," *IEEE Trans. Geosci. Remote Sens.*, vol. 47, no. 12, pp. 4143–4152, Dec. 2009.

[15] M. Dabboor, V. Karathanassi, and A. Braun, "Multilevel hierarchical segmentation method for polarimetric SAR data based on scattering behaviour and histograms," *Can. J. Remote Sens.*, vol. 36, no. 2, pp. 142–153, 2010.

[16] R. Lucas, J. Armston, R. Fairfax, R. Fensham, A. Accad, J. Carreiras, J. Kelley, P. Bunting, D. Clewley, S. Bray, D. Metcalfe, J. Dwyer, M. Bowen, T. Eyre, M. Laidlaw, and M. Shimada, "An evaluation of the ALOS PALSAR L-band backscatter—Above ground biomass relationship Queensland, Australia: Impacts of surface moisture condition and vegetation structure," *IEEE J. Sel. Topics Appl. Earth Obs. Remote Sens.*, vol. 3, no. 4, pp. 576–593, Dec. 2010.

[17] W. S. Walker, C. M. Stickler, J. M. Kellndorfer, K. M. Kirsch, and D. C. Nepstad, "Large-area classification and mapping of forest and land cover in the Brazilian Amazon: A comparative analysis of ALOS/PALSAR and Landsat data sources," *IEEE J. Sel. Topics Appl. Earth Obs. Remote Sens.*, vol. 3, no. 4, pp. 594–604, Dec. 2010.

[18] M. Shimada, "Model-based polarimetric SAR calibration method using forest and surface-scattering targets," *IEEE Trans. Geosci. Remote Sens.*, vol. 49, no. 5, pp. 1712–1733, May 2011.

[19] C. Wang, J. Wu, Y. Zhang, G. Pan, J. Qi, and W. A. Salas, "Characterizing L-band scattering of paddy rice in southeast China with radiative transfer model and multitemporal ALOS/PALSAR imagery," *IEEE Trans. Geosci. Remote Sens.*, vol. 47, no. 4, pp. 988–998, Apr. 2009.

[20] D. H. Hoekman, M. Vissers, and N. Wielaard, "PALSAR wide-area mapping of Borneo: Methodology and map validation," *IEEE J. Sel. Topics Appl. Earth Obs. Remote Sens.*, vol. 3, no. 4, pp. 605–617, Dec. 2010.

[21] H. T. Chu and L. Ge, "Synergistic use of multi-temporal ALOS/PALSAR and SPOT multi-spectral satellite imagery for land cover mapping in the Ho Chi Minh city area, Vietnam," in *Proc. IGARSS*, Honolulu, HI, Jul. 2010, pp. 1465–1468.

[22] H. Bagan, Y. Yasuoka, T. Endo, X. Wang, and Z. Feng, "Classification of airborne hyperspectral data based on the average learning subspace method," *IEEE Geosci. Remote Sens. Lett.*, vol. 5, no. 3, pp. 368–372, Jul. 2008.

[23] A. Jain, R. Duin, and J. Mao, "Statistical pattern recognition: A review," *IEEE Trans. Pattern Anal. Mach. Intell.*, vol. 22, no. 1, pp. 4–37, Jan. 2000.

[24] M. Pal and G. M. Foody, "Feature selection for classification of hyperspectral data by SVM," *IEEE Trans. Geosci. Remote Sens.*, vol. 48, no. 5, pp. 2297–2307, May 2010.

[25] T. M. Lillesand, R. W. Kiefer, and J. W. Chipman, *Remote Sensing and Image Interpretation*., 5th ed. Hoboken, NJ: Wiley, 2004.

[26] M. Shimada, O. Isoguchi, T. Tadono, and K. Isono, "PALSAR radiometric and geometric calibration," *IEEE Trans. Geosci. Remote Sens.*, vol. 47, no. 12, pp. 3915–3932, Dec. 2009.

[27] A. B. Kostinski and W.-M. Boerner, "On foundations of radar polarimetry," *IEEE Trans. Antennas Propag.*, vol. AP-34, no. 12, pp. 1395–1404, Dec. 1986.

[28] S. R. Cloude, *Polarisation: Applications in Remote Sensing*. New York: Oxford Univ. Press, 2010.

[29] E. Oja, *Subspace Methods of Pattern Recognition*. Letchworth, U.K.: Res. Stud. Press and Wiley, 1983.

[30] M. V. Jankovic and H. Ogawa, "Modulated Hebb–Oja learning rule—A method for principal subspace analysis," *IEEE Trans. Neural Netw.*, vol. 17, no. 2, pp. 345–356, Mar. 2006.

[31] H. Bagan, W. Takeuchi, Y. Yamagata, X. Wang, and Y. Yasuoka, "Extended averaged learning subspace method for hyperspectral data classification," *Sensors*, vol. 9, no. 6, pp. 4247–4270, Jun. 2009.

[32] H. Bagan and Y. Yamagata, "Improved subspace classification method for multispectral remote sensing image classification," *Photogramm. Eng. Remote Sens.*, vol. 76, no. 11, pp. 1239–1251, Nov. 2010.

[33] T. Maeda, "Bird use of rice field strips of varying width in the Kanto Plain of central Japan," *Agric. Ecos. Environ.*, vol. 105, no. 1/2, pp. 347–351, Jan. 2005.

[34] R. G. Congalton and K. Green, *Assessing the Accuracy of Remotely Sensed Data: Principles and Practices*. Boca Raton, FL: Lewis Publishers, 1999.

[35] C. W. Hsu, C. C. Chang, and C. J. Lin, A practical guide to support vector classification, Dept. Comput. Sci., Nat. Taiwan Univ., Taipei, Taiwan, Tech. Rep. [Online]. Available: http://www.csie.ntu.edu.tw/~cjlin/papers/guide/guide.pdf

[36] T. Habib, J. Inglada, G. Mercier, and J. Chanussot, "Support vector reduction in SVM algorithm for abrupt change detection in remote sensing," *IEEE Geosci. Remote Sens. Lett.*, vol. 6, no. 3, pp. 606–610, Jul. 2009.

[37] B. Waske, S. van der Linden, J. A. Benediktsson, A. Rabe, and P. Hostert, "Sensitivity of support vector machines to random feature selection in classification of hyperspectral data," *IEEE Trans. Geosci. Remote Sens.*, vol. 48, no. 7, pp. 2880–2889, Jul. 2010.

[38] G. Mountrakis, J. Im, and C. Ogole, "Support vector machines in remote sensing: A review," *ISPRS J. Photogramm. Remote Sens.*, vol. 66, no. 3, pp. 247–259, May 2011.

[39] S. S. Keerthi and C.-J. Lin, "Asymptotic behaviors of support vector machines with Gaussian kernel," *Neural Comput.*, vol. 15, no. 7, pp. 1667–1689, Jul. 2003.

Hasi Bagan (M'07) received the B.S. degree in mathematics from Peking University, Beijing, China, in 1991, the M.S. degree in mathematics from the Beijing University of Aeronautics and Astronautics, Beijing, in 1996, and the Ph.D. degree from the Institute of Remote Sensing Applications, Chinese Academy of Sciences, Beijing, in 2004.

From 2004 to 2006, he was a Postdoctoral Researcher with the National Institute for Environmental Studies, Tsukuba, Japan. From 2006 to 2008, he was a Japan Society for the Promotion of Science Postdoctoral Fellow with the Institute of Industrial Science, The University of Tokyo, Tokyo, Japan. He is currently a Research Associate with the National Institute for Environmental Studies. His research interests include land cover classification, neural networks, wavelet fusion, and subspace algorithms.

Tsuguki Kinoshita received the B.Eng. degree, the M.Eng. degree in naval architecture, and the Dr.Eng. degree from The University of Tokyo, Tokyo, Japan, in 1993, 1996, and 1999, respectively.

He is currently an Associate Professor with the College of Agriculture, Ibaraki University, Ami, Japan. His research topic is global land use modeling and woody biomass potential survey. He is also a Member of the Representative Concentration Pathways task team.

Yoshiki Yamagata received the B.S. degree in system science and the Ph.D. degree from The University of Tokyo, Tokyo, Japan, in 1985 and 1997, respectively.

From 1985 to 1991, he was a Researcher with the National Institute for Agro-Environmental Sciences, Tsukuba, Japan. In 1991, he joined the National Institute for Environmental Studies, Tsukuba, where he was a Senior Researcher and then a Research Manager and is currently a Special Senior Researcher with the Center for Global Environmental Research. He serves as an Editor of *Climate Policy*, *Environmental Science & Policy*, and *Applied Energy*. His major research fields are remote sensing, geographic information system, and spatial data analysis for environment and disaster assessment.

Dr. Yamagata was the recipient of the First Oze Prize in 1998 and the Paper Award from the Japan Simulation Society in 2006.